Multi-Species Collisions for Delta-F Gyrokinetic Simulations: Implementation and Validation with GENE

P. Crandall[1,*,†], D. Jarema[2], H. Doerk[2], Q. Pan[3], G. Merlo[4]
T. Görler[2], A. Bañón Navarro[2], D. Told[2], M. Maurer[2], F. Jenko[2,4]

November 13, 2018

[1]Department of Physics and Astronomy, University of California, Los Angeles, California 90095, USA
[2]Max-Planck-Institut für Plasmaphysik, Boltzmannstrasse 2, 85748 Garching, Germany
[3]Plasma Science and Fusion Center, Massachusetts Institute of Technology, Cambridge, Massachusetts 02139, USA
[4]University of Texas at Austin, Austin, Texas 78712, USA
[*]pcrandall@ucla.edu
[†]Postal Address: Boltzmannstrasse 2, 85748 Garching, Germany

Abstract

A multi-species linearized collision operator based on the model developed by Sugama et al. has been implemented in the nonlinear gyrokinetic code, GENE. Such a model conserves particles, momentum, and energy to machine precision, and is shown to have negative definite free energy dissipation characteristics, satisfying Boltzmann's H-theorem, including for realistic mass ratio. Finite Larmor Radius (FLR) effects have also been implemented into the local version of the code. For the global version of the code, the collision operator has been developed to allow for block-structured velocity space grids, allowing for computationally tractable collisional global simulations. The validity of the collision operator has been demonstrated by relaxation tests, neoclassical simulations, comparisons of the simulated damping of zonal flows with theoretical predictions, and a microinstability benchmark. The newly implemented operator shall be used in future simulations to study plasma turbulence and transport in the highly collisional edge.

1 Introduction

Any realistic simulation of plasma turbulence near the edge of fusion devices such as tokamaks or stellarators must include more than just the collective motion of particles and the evolution of the electromagnetic fields based on the Maxwell equations. To more realistically model the plasma behavior, one must include discrete particle effects, where the ions and electrons occasionally interact with each other, and not just the fields arising from the bulk motion of particles. These effects act as an important sink of free energy and contribute to the dampening/growth of certain plasma instabilities. Within the core of fusion devices, particles may be at a high enough temperature such that when they cross near each other, they would go by at a high enough speed that they have little time for the interactions to play much of a role. This is certainly not true in the edge, where one encounters lower

temperatures. For this reason, a collision operator which models the physics of such interactions has been implemented in the GENE code [1, 2] to study plasma turbulence and transport in the edge.

Many different collision operators have been derived in the literature for use with gyrokinetic models, see Ref. [3, 4, 5, 6, 7, 8, 9]. Different codes may use different collision operators depending on whether they are delta-f/full-f and Eulerian/Lagrangian/Semi-Lagrangian codes. A diverse selection of collision operators have been implemented in ORB5 [10], GYSELA [11], XGC [12], GKW [13], GKV [14], GS2 [15], and more.

GENE is a delta-f grid-based code and the collision operator implemented in GENE is based on the model derived by Sugama et al. [3]. The model contains no velocity-space convolution integrals, and its linear nature allows for optimized time-stepping schemes. Furthermore, the use of the local flux-tube approximation, as well as the recently developed block-structured velocity space grids [16, 17] for the global version of the code, allow for the capability of collisional gyrokinetic simulations without the need for the large velocity space resolution that would inhibit other gyrokinetic codes. The amount of physics contained within the operator (pitch-angle scattering, energy diffusion, FLR corrections, etc.), as well as its good numerical properties (particle, momentum, and energy conservation, as well as free energy dissipation) and computational tractability allow for unique, cutting-edge simulations exploring collisional plasma turbulence in the edge.

This paper is outlined as follows: Section 2 describes the analytical model for the collision operator implemented in GENE. Section 3 describes the numerical implementation of the collision operator in GENE. The numerical implementation is based on a second-order finite volume scheme as opposed to the implementation described in [14] which is based on a finite difference scheme. Section 4 presents the results of tests that verify that the operator behaves as expected for realistic mass ratio systems. This includes relaxation and conservation tests, neoclassical tests, a study of the effects of collisions on zonal flows, and a microinstability benchmark. Conclusions are drawn in section 5.

2   Analytical collision model used in GENE

The previous linearized Landau-Boltzmann collision operator implemented in GENE and documented in [18] and [19] has been upgraded to a linearized Sugama collision operator [3] to ensure that an appropriate H-theorem is satisfied for a nonisothermal parameter set. With these modifications, the change in free energy in the system by collisions is guaranteed to be negative definite. In addition, the collision operator has been refactored to incorporate FLR corrections in the local version of the code. The task of upgrading collisional FLR corrections for use with the global version of the code will be left for future work.

2.1   Assumptions and use of models in collisional dissipation term

Since GENE is a delta-f gyrokinetic code, the collisions must evolve the perturbed distribution while keeping the background distribution fixed. As such, the collisional dissipation term is split into four parts:

$$C_{ab}(F_a, F_b) = C_{ab}(F_{Ma}, F_{Mb}) + C_{ab}(f_a, F_{Mb}) + C_{ab}(F_{Ma}, f_b) + O(\epsilon^2) \qquad (1)$$

The first term is responsible for the equilibration of the background distributions, and is neglected in the model because it is assumed to be small, and because the background profiles are regarded as fixed throughout the course of the simulation. The last nonlinear term is also neglected because it is

assumed to be of second order importance in the model. The second term, $C_{ab}(f_a, F_{Mb})$, is called the test-particle part of the collision operator, $C_{ab}^T(f_a)$, and can be interpreted as the term which modifies the perturbed distribution function, f_a, as a result of collisions with the background, F_{Mb}. For a linearized Landau-Boltzmann collision operator, the test-particle part is given by:

$$C_{ab}^T(f_a) = C_{ab}^{T0}(f_a) + \frac{m_a}{T_b}\left(1 - \frac{T_b}{T_a}\right)\frac{1}{v^2}\frac{\partial}{\partial v}\left(\frac{\nu_\parallel^{ab}(v)}{2}v^5 f_a\right) \tag{2}$$

In the above expression, m_a and T_a represent the mass and temperature of species a, respectively. The radial velocity space coordinate is given by v. C_{ab}^{T0} is given by:

$$C_{ab}^{T0}(f_a) = \nu_D^{ab}(v)\mathfrak{L}f_a + \frac{1}{v^2}\frac{\partial}{\partial v}\left(\frac{v^4}{2}\nu_\parallel^{ab}(v)F_{Ma}\frac{\partial}{\partial v}\left(\frac{f_a}{F_{Ma}}\right)\right) \tag{3}$$

For the purposes of transparency, a similar notation to Ref. [3] has been used. In the above expression, $\nu_D^{ab}(v)$ and $\nu_\parallel^{ab}(v)$ represent the pitch-angle scattering and energy diffusion frequency respectively. The pitch-angle scattering operator is deonoted by $\mathfrak{L}$. The test-particle part has been separated into a part which is self-adjoint, C_{ab}^{T0}, and a part which only exists for a nonisothermal case, and which breaks self-adjointness symmetry. The latter term can be responsible for the creation of free energy in the system. This is because when the collision operator was linearized, the background was regarded as fixed compared to the perturbations, and that leads to a complication. In the isothermal case, free energy would always flow from the perturbation to the Maxwellian background distribution, otherwise the second law of thermodynamics would be violated. However, if the background distributions are at different temperatures, then free energy can flow from the background distribution of one species to the perturbation of another species. For a situation where the background is kept fixed, this can result in free energy flowing into the system.

It is highly desirable to have a collision operator which acts as a pure sink of free energy and satisfies an H-theorem. Otherwise, one may observe numerical instabilities in any simulation which uses collisions. For this reason, the test-particle operator is replaced with a model term which satisfies an H-theorem and has a collisional asymptotic limit which is a generalization of the isothermal one. For an isothermal case with a linearized Landau-Boltzmann operator, all perturbations are driven to a distribution of the form:

$$f_a \to F_{Ma}\left(\frac{\delta n_a}{n_a} + \frac{m_a}{T_a}u_\parallel v_\parallel + \frac{\delta T}{T}\left(\frac{v^2}{v_{Ta}^2} - \frac{3}{2}\right)\right) \tag{4}$$

where $u_\parallel$ and $\delta T/T$ is the same between all species in the relaxed state. This property holds in the isothermal case, and the Sugama collisional model is constructed such that this holds also in the nonisothermal case. In creating such a model, the above formula is regarded as the collisional equilibrium for simulations where the background distributions are fixed, even though it is not a true thermal equilibrium.

The Sugama operator is constructed by replacing the nonisothermal problematic term with a new model term. In the limit of very small mass ratio (in practical simulations, all of the ion species are considered to have the same temperature, so very small mass ratio always applies), this term vanishes for electron-ion collisions but not for ion-electron collisions. So the model is weighted by a mass and temperature dependent coefficient that vanishes for electron-ion collisions. For the case of ion-electron collisions, the model is constructed such that it gives the same momentum and free energy transfer (not the same total energy transfer) as the original term, as well as satisfying the appropriate symmetry

3

relations (explained in more detail in subsection 2.3). By disregarding the complete energy transfer and focusing solely on free energy transfer, the nonisothermal parameter set is essentially regarded as an equilibrium for the simulation. While this is not a true thermal equilibrium, thermalization occurs on much larger time scales than gyrokinetic transport phenomena, and can be neglected in a simulation. Furthermore, in any simulation which considers the background profiles as fixed, the thermalization should be neglected, otherwise one would have a collision operator that does not reliably drive perturbations to a simple final state.

The third term in Eq. (1), $C_{ab}(F_{Ma}, f_b)$, is called the field-particle part of the collision operator, $C_{ab}^F(f_b)$. This term represents the evolution of a Maxwellian due to collisions with a perturbation. Again, since the background distributions have been regarded as fixed, it is not clear how one should model the effects of such a term. Furthermore, the computation of such a term would be expensive due to the nonlocal velocity space integral (the analytical model for this has been done by [5]). However, if one were to ignore such a term, then the model collision operator would be unable to satisfy the essential conservation laws for momentum and energy:

$$\int d^3v\, m_a \mathbf{v} C_{ab} = -\int d^3v\, m_b \mathbf{v} C_{ba} \tag{5}$$

$$\int d^3v\, \frac{1}{2} m_a v^2 C_{ab} = -\int d^3v\, \frac{1}{2} m_b v^2 C_{ba} \tag{6}$$

For these reasons, the second term is replaced with a model operator such that the collision operator as a whole conserves momentum and energy:

$$C_{ba}^F(f_a) = -\frac{T_a}{T_b} \frac{C_{ba}^T\left(\frac{F_{Mb} m_b \mathbf{v}}{T_b}\right) \cdot \int d^3v\, \frac{m_a \mathbf{v}}{T_a} C_{ab}^T(f_a)}{\int d^3v\, \frac{m_b v_\parallel}{T_b} C_{ba}^T(F_{Mb} m_b v_\parallel / T_b)} - \frac{T_a}{T_b} \frac{C_{ba}^T(F_{Mb} x_b^2) \int d^3v\, x_a^2 C_{ab}^T(f_a)}{\int d^3v\, x_b^2 C_{ba}^T(F_{Mb} x_b^2)} \tag{7}$$

The complete linearized collision operator thus consists of the test-particle part and the field-particle part:

$$C_{ab}^{linear}(f_a, f_b) = C_{ab}^T(f_a) + C_{ab}^F(f_b) \tag{8}$$

To account for FLR corrections, the distribution function is transformed from guiding center to particle coordinates with the pull-back operator, $T_{gc \to p}$, acted on by the collision operator, transformed from particle to guiding center coordinates with the inverse operator, $T_{p \to gc}$, and then gyroaveraged:

$$C_{ab}^{GK} = \oint \frac{d\phi}{2\pi} T_{p \to gc} C_{ab}^{linear}\left(T_{gc \to p} f_a, T_{gc \to p} f_b\right) \tag{9}$$

In principle, such transformations should be done between particle and gyrocenter coordinates, rather than guiding center coordinates. However, considering such terms would severely complicate the analytical model and numerical implementation. Furthermore, it is not clear that adding such additional terms makes sense when other terms have already been replaced with ad-hoc model operators. Nevertheless, the development of the analytical and numerical theory of more advanced gyrokinetic collision operators is still an open problem in the community.

One may wonder whether the use of such assumptions and models is justified. It has been argued that the exact form for collisions does not matter, as long as a sink of free energy is present. It could be that as long as pitch-angle scattering and energy diffusion are retained in the operator, then the other terms as well as the exact size of the free energy sink are not as important, so long as appropriate

conservation and symmetry properties are retained to prevent numerical instabilities in the model. In addition, in the limit of very small mass ratio, only the ion-electron term is affected in the test-particle part of the Sugama collision operator. Since ions are far heavier than electrons, the exact functional form of the ion-electron collision operator should not matter much provided that conservation and symmetry properties are maintained.

To truly determine the validity of the collision operator, however, requires a comparison with a full-f code with a more complete collision model. This has already been done for a neoclassical scenario in [20] for an isothermal parameter set. The agreement between the neoclassical moments in that case has been found to be reasonably good (the heat and particle fluxes have been found to agree within $\sim 20\%$). The full analytical form of the collision operator implemented in GENE is displayed in the following subsection.

2.2 Sugama collision model implemented in GENE

The full gyrokinetic collision operator in the local limit takes the following form (the notation used for the operator is the same as in [14], which describes another implementation of the Sugama collision operator):

$$C_{ab}^{(Gyrokinetic)}(h_{a\mathbf{k}_\perp}, h_{b\mathbf{k}_\perp}) = C_{ab}^{T0}(h_{a\mathbf{k}_\perp}) - \frac{k_\perp^2 h_{a\mathbf{k}_\perp}}{4\Omega_a^2}(\nu_D^{ab}(v)(2v_\parallel^2 + v_\perp^2) + \nu_\parallel^{ab}(v)v_\perp^2)$$

$$+ \sum_{n=1}^{6}(X_{n\mathbf{k}_\perp}^{ab} M_{n\mathbf{k}_\perp}^{ab} + Y_{n\mathbf{k}_\perp}^{ab} M_{n\mathbf{k}_\perp}^{ba}) \tag{10}$$

The component parts of C_{ab}^{T0} and the spatial diffusion are defined as follows:

$$\nu_D^{ab}(v) = \frac{4\pi n_b}{m_a^2 v^3} e_a^2 e_b^2 \ln(\Lambda)(\Phi(x_b) - G(x_b)) \tag{11}$$

$$\nu_\parallel^{ab}(v) = \frac{8\pi e_a^2 e_b^2 \ln(\Lambda) n_b}{m_a^2 v^3} G(x_b) \tag{12}$$

$$C_{ab}^{T0}(f_a) = \nu_D^{ab}(v)\mathfrak{L}f_a + \frac{1}{v^2}\frac{\partial}{\partial v}\left(\frac{v^4}{2}\nu_\parallel^{ab}(v)F_{Ma}\frac{\partial}{\partial v}\left(\frac{f_a}{F_{Ma}}\right)\right) \tag{13}$$

$$\mathfrak{L} = \frac{1}{2}\frac{\partial}{\partial \mathbf{v}} \cdot \left(v^2\overleftrightarrow{\mathbf{I}} - \mathbf{vv}\right) \cdot \frac{\partial}{\partial \mathbf{v}} = \frac{1}{2}\left(\frac{1}{\sin(\theta)}\frac{\partial}{\partial \theta}sin(\theta)\frac{\partial}{\partial \theta} + \frac{1}{\sin^2(\theta)}\frac{\partial^2}{\partial \phi^2}\right) \tag{14}$$

In the expression for the pitch-angle scattering operator given above, $\overleftrightarrow{\mathbf{I}}$ represents the velocity space identity tensor. The six integral moments that are calculated for the collision operator are given by:

$$M_{1\mathbf{k}_\perp}^{ab} = \int d^3v \frac{m_a v_\parallel}{T_a} C_{ab}^{T0}(J_0(k_\perp \rho_a)h_{a\mathbf{k}_\perp}) \tag{15}$$

$$M_{2\mathbf{k}_\perp}^{ab} = \int d^3v \frac{m_a v_\parallel}{T_a} C_{ab}^{T0}(J_1(k_\perp \rho_a)h_{a\mathbf{k}_\perp} v_\perp/v_\parallel) \tag{16}$$

$$M_{3\mathbf{k}_\perp}^{ab} = \int d^3v x_a^2 C_{ab}^{T0}(J_0(k_\perp \rho_a)h_{a\mathbf{k}_\perp}) \tag{17}$$

$$M_{4\mathbf{k}_\perp}^{ab} = \int d^3v v_\parallel J_0(k_\perp \rho_a)h_{a\mathbf{k}_\perp} \tag{18}$$

$$M_{5\mathbf{k}_\perp}^{ab} = \int d^3v v_\perp J_1(k_\perp \rho_a)h_{a\mathbf{k}_\perp} \tag{19}$$

$$M_{6\mathbf{k}_\perp}^{ab} = \int d^3v J_0(k_\perp \rho_a)h_{a\mathbf{k}_\perp}\left(x_a^2 - \frac{3}{2}\right) \tag{20}$$

The six coefficients of the moments for the test-particle part are given by:

$$X_{1\mathbf{k}_\perp}^{ab} = (\theta_{ab} - 1)J_0(k_\perp \rho_a)F_{Ma}\frac{v_\parallel}{n_a} \tag{21}$$

$$X_{2\mathbf{k}_\perp}^{ab} = (\theta_{ab} - 1)J_1(k_\perp \rho_a)F_{Ma}\frac{v_\perp}{n_a} \tag{22}$$

$$X_{3\mathbf{k}_\perp}^{ab} = (\theta_{ab} - 1)J_0(k_\perp \rho_a)F_{Ma}(x_a^2 - \frac{3}{2})\frac{2}{3n_a} \tag{23}$$

$$X_{4\mathbf{k}_\perp}^{ab} = (\theta_{ab} - 1)J_0(k_\perp \rho_a)\frac{1}{\theta_{ab}n_a}C_{ab}^{TS}\left(\frac{F_{Ma}m_a v_\parallel}{T_a}\right) \tag{24}$$

$$X_{5\mathbf{k}_\perp}^{ab} = \frac{J_1(k_\perp \rho_a)v_\perp}{J_0(k_\perp \rho_a)v_\parallel}X_{4\mathbf{k}_\perp}^{ab} \tag{25}$$

$$X_{6\mathbf{k}_\perp}^{ab} = (\theta_{ab} - 1)J_0(k_\perp \rho_a)\frac{2}{3\theta_{ab}n_a}C_{ab}^{TS}(F_{Ma}x_a^2) \tag{26}$$

The six coefficients of the transposed moments for the field-particle part are given by:

$$Y_{1\mathbf{k}_\perp}^{ab} = -\frac{T_b\theta_{ba}}{\gamma_{ab}}C_{ab}^{TS}(F_{Ma}\frac{m_a v_\parallel}{T_a})J_0(k_\perp \rho_a) \tag{27}$$

$$Y_{2\mathbf{k}_\perp}^{ab} = \frac{J_1(k_\perp \rho_a)v_\perp}{J_0(k_\perp \rho_a)v_\parallel}Y_{1\mathbf{k}_\perp}^{ab} \tag{28}$$

$$Y_{3\mathbf{k}_\perp}^{ab} = -\frac{T_b\theta_{ba}}{\eta_{ab}}C_{ab}^{TS}(F_{Ma}x_a^2)J_0(k_\perp \rho_a) \tag{29}$$

$$Y_{4\mathbf{k}_\perp}^{ab} = -\frac{m_b\alpha_{ba}\theta_{ba}}{\tau_{ba}T_b\sqrt{1+\alpha_{ba}^2}}Y_{1\mathbf{k}_\perp}^{ab} \tag{30}$$

$$Y_{5\mathbf{k}_\perp}^{ab} = -\frac{m_b\alpha_{ba}\theta_{ba}}{\tau_{ba}T_b\sqrt{1+\alpha_{ba}^2}}Y_{2\mathbf{k}_\perp}^{ab} \tag{31}$$

$$Y_{6\mathbf{k}_\perp}^{ab} = -\frac{2\alpha_{ba}\theta_{ba}}{\tau_{ba}(1+\alpha_{ba}^2)^{3/2}}Y_{3\mathbf{k}_\perp}^{ab} \tag{32}$$

The other miscellaneous terms needed for the coefficients of the moments are defined as follows:

$$C_{ab}^{TS}\left(F_{Ma}\frac{m_a v_\parallel}{T_a}\right) = \theta_{ab}\left(C_{ab}^{T0}\left(F_{Ma}\frac{m_a v_\parallel}{T_a}\right) - \frac{F_{Ma}m_a\alpha_{ab}v_\parallel(\theta_{ab}-1)}{\tau_{ab}T_a\sqrt{1+\alpha_{ab}^2}}\right) \tag{33}$$

$$C_{ab}^{TS}(F_{Ma}x_a^2) = \theta_{ab}\left(C_{ab}^{T0}(F_{Ma}x_a^2) - \frac{2F_{Ma}\alpha_{ab}(\theta_{ab}-1)}{\tau_{ab}(1+\alpha_{ab}^2)^{3/2}}\left(x_a^2 - \frac{3}{2}\right)\right) \tag{34}$$

$$\theta_{ab} = \sqrt{\frac{T_a(m_a+m_b)}{(T_a m_b + T_b m_a)}} \tag{35}$$

$$\alpha_{ab} = v_{Ta}/v_{Tb} \tag{36}$$

$$\gamma_{ab} = T_a\int d^3v\frac{m_a v_\parallel}{T_a}C_{ab}^{TS}\left(F_{Ma}\frac{m_a v_\parallel}{T_a}\right) \tag{37}$$

$$\eta_{ab} = T_a\int d^3v x_a^2 C_{ab}^{TS}(F_{Ma}x_a^2) \tag{38}$$

$$\frac{3\sqrt{\pi}}{4\tau_{ab}} = \frac{2\gamma_{ab}n_b}{m_a^2 v_{Ta}^3} = \frac{4\pi n_b e_a^2 e_b^2\ln(\Lambda)}{m_a^2 v_{Ta}^3} \tag{39}$$

$$F_{Ma} = \frac{n_a}{(\sqrt{\pi}v_{Ta})^3}e^{-(\frac{v}{v_{Ta}})^2} \tag{40}$$

In the above expressions, $\mathbf{k}_\perp$ denotes the perpendicular wavenumber, $h_{a\mathbf{k}_\perp}$ denotes the nonadiabatic part of the perturbed distribution function, Ω_a denotes the cyclotron frequency of species a, $v_\parallel$ denotes the parallel velocity, $v_\perp$ denotes the perpendicular velocity, n_a denotes the density of species a, m_a denotes the mass of species a, v denotes the speed, T_a denotes the temperature of species a, $v_{Ta} = \sqrt{2T_a/m_a}$ denotes the thermal velocity of species a, $x_a = v/v_{Ta}$ denotes the speed normalized to the thermal velocity, e_a denotes the charge of species a, $\ln(\Lambda)$ denotes the coloumb logarithm, $\Phi(x)$ denotes the error function, $G(x) = (\Phi(x) - x\Phi'(x))/2x^2$ denotes the Chandrasekhar function, J_0 and J_1 represent the zeroth and first order Bessel functions of the first kind respectively, and ρ_a denotes the gyroradius of species a.

The gyrokinetic collision operator for the global version of the code is similar to the local version, except that the zeroth order bessel function is set to 1, the first order bessel function is set to 0, and the term proportional to $k_\perp^2$ is neglected. All that is needed to extend the FLR corrections to the global version of such an operator is to generalize the bessel functions to gyroaverage matrices and to generalize the spatial diffusion term to include derivatives in configuration space. The extension of the global version of the collision operator to include FLR effects shall be left for future work.

2.3   Properties of the collision operator

The collision operator obtained satisfies conservation of particles, momentum, and energy in the drift-kinetic limit $(k_\perp \to 0)$:

$$\int d^3v C_{ab} = 0 \tag{41}$$

$$\int d^3v\, m_a \mathbf{v} C_{ab} = -\int d^3v\, m_b \mathbf{v} C_{ba} \tag{42}$$

$$\int d^3v\, \frac{1}{2} m_a v^2 C_{ab} = -\int d^3v\, \frac{1}{2} m_b v^2 C_{ba} \tag{43}$$

In addition, the test-particle and field-particle parts of the collision operator satisfy the following symmetry relations:

$$\int d^3v\, \frac{f_a}{F_{Ma}} C_{ab}^T(g_a) = \int d^3v\, \frac{g_a}{F_{Ma}} C_{ab}^T(f_a) \tag{44}$$

$$T_a \int d^3v\, \frac{f_a}{F_{Ma}} C_{ab}^F(f_b) = T_b \int d^3v\, \frac{f_b}{F_{Mb}} C_{ba}^F(f_a) \tag{45}$$

With these symmetry relations, the following H-theorem can be obtained:

$$T_a \int d^3v\, \frac{f_a}{F_{Ma}} C_{ab} + T_b \int d^3v\, \frac{f_b}{F_{Mb}} C_{ba} \leq 0 \tag{46}$$

The differential part of the collision operator will tend to smooth out fine-scale velocity space structures, and the pitch-angle scattering in the opertator will tend to make the distribution more isotropic. The asymptotic state of the collision operator (assuming no other terms are present) is a perturbed Maxwellian in the drift-kinetic limit:

$$f_a \to F_{Ma}\left(\frac{\delta n_a}{n_a} + \frac{m_a}{T_a} u_\parallel v_\parallel + \frac{\delta T}{T}\left(\frac{v^2}{v_{Ta}^2} - \frac{3}{2} \right) \right) \tag{47}$$

Where $u_\parallel$ and $\delta T/T$ is the same between all species in the relaxed state. In addition, the spatial diffusion term from the FLR corrections will tend to dampen small scale configuration space structures perpendicular to the magnetic field.

3 Numerical implementation of gyrokinetic collision operator

The collision operator is discretized such that particles, momentum, and energy are conserved to machine precision in the drift-kinetic limit ($k_\perp \to 0$) where it is simple to write down the appropriate conservation laws, and then the scheme is generalized to incorporate FLR effects. The updated collision operator in GENE is designed such that it acts on the nonadiabatic part of the perturbed distribution divided by the background Maxwellian. The division by the background Maxwellian is done to numerically ensure the following self-adjointness relation:

$$\int d^3v\, \frac{f_a}{F_{Ma}} C_{ab}^{T0}(g_a) = \int d^3v\, \frac{g_a}{F_{Ma}} C_{ab}^{T0}(f_a) \tag{48}$$

And the nonadiabatic part of the distribution is used because the rate of change of free energy, $dF/dt|_{coll}$, is defined from the nonadiabatic part of the distribution [21]:

$$\left. \frac{dF}{dt} \right|_{coll} = \sum_j n_j T_j \int d^3v\, \frac{h_j}{F_{Mj}} C_j \tag{49}$$

8

So to numerically ensure the appropriate symmetry properties and H-theorem, the nonadiabatic distribution, h_a, must be used. FLR corrections have only been implemented into the local version of the GENE code, where the coordinates corresponding to the configuration space perpendicular to the magnetic field are evaluated in fourier space. Extending FLR corrections to the global version of the code will be left for future work.

3.1   Numerical Implementation of differential test-particle part

The test-particle part, $C_{ab}^{T0}(h_a)$, is evaluated with a second order finite volume scheme on a grid which is equidistant in parallel and perpendicular velocity. The collisional fluxes are evaluated on a staggered velocity space grid from the nonadiabatic part of the distribution function divided by a background Maxwellian distribution. For this purpose, C_{ab}^{T0} (Eq. (3)) is written in a form more amenable to a finite volume discretization:

$$C_{ab}^{T0}(h_a) = \nabla_v \cdot \mathbf{J}_{ab} \tag{50}$$

Where the collisional 2D velocity subspace flux, $\mathbf{J}_{ab}$, can be split into a pitch-angle scattering part and an energy diffusion part:

$$\mathbf{J}_{ab} = \mathbf{J}_{ab,pa} + \mathbf{J}_{ab,ed} \tag{51}$$

$$\mathbf{J}_{ab,pa} = \frac{\nu_D(v)}{2}\left(v^2 \overleftrightarrow{\mathbf{I}} - \mathbf{vv}\right)F_{Ma} \cdot \frac{\partial}{\partial \mathbf{v}}\left(\frac{h_a}{F_{Ma}}\right) \tag{52}$$

$$\mathbf{J}_{ab,ed} = \frac{v}{2}\nu_{\parallel}^{ab}(v)F_{Ma}\frac{\partial}{\partial v}\left(\frac{h_a}{F_{Ma}}\right)\mathbf{v} \tag{53}$$

From the above expression, it is straightforward to split the collisional flux into a parallel and a perpendicular part:

$$J_{ab}^{\parallel} = \frac{1}{2}\left(v_{\parallel}^2\nu_{\parallel}^{ab}(v) + v_{\perp}^2\nu_D^{ab}(v)\right)F_{Ma}\frac{\partial}{\partial v_{\parallel}}\left(\frac{h_a}{F_{Ma}}\right) + \frac{1}{2}\left(\nu_{\parallel}^{ab}(v) - \nu_D^{ab}(v)\right)v_{\parallel}v_{\perp}F_{Ma}\frac{\partial}{\partial v_{\perp}}\left(\frac{h_a}{F_{Ma}}\right) \tag{54}$$

$$J_{ab}^{\perp} = \frac{1}{2}\left(\nu_{\parallel}^{ab}(v) - \nu_D^{ab}(v)\right)v_{\parallel}v_{\perp}F_{Ma}\frac{\partial}{\partial v_{\parallel}}\left(\frac{h_a}{F_{Ma}}\right) + \frac{1}{2}\left(v_{\perp}^2\nu_{\parallel}^{ab}(v) + v_{\parallel}^2\nu_D^{ab}(v)\right)F_{Ma}\frac{\partial}{\partial v_{\perp}}\left(\frac{h_a}{F_{Ma}}\right) \tag{55}$$

All of the frequencies and the background distribution are evaluated on the staggered grid (if the standard velocity space coordinates are evaluated from the indices 0, 1, 2, etc., then the staggered velocity space coordinates are evaluated from the indices 0.5, 1.5, 2.5, etc.) and the derivatives are interpolated to the staggered grid as follows:

$$\frac{\partial g}{\partial v_{\parallel}}\bigg|_{(l+1/2),(m+1/2)} = \frac{1}{2\Delta v_{\parallel}}\left(g(l+1,m) - g(l,m)\right) + \frac{1}{2\Delta v_{\parallel}}\left(g(l+1,m+1) - g(l,m+1)\right) \tag{56}$$

The use of the staggered grid is part of the second-order finite volume scheme implementation. In the above expression, $v_{\parallel}$ is indexed by l and $v_{\perp}$ is indexed by m. The derivatives with respect to $v_{\perp}$

are defined in an analogous manner. The collision operator on the standard grid is then evaluated numerically from the staggered fluxes as:

$$C_{ab}^{T0}(h_a) = \left(J_{ab}^{\parallel}(l+1/2, m) - J_{ab}^{\parallel}(l-1/2, m) \right)/\Delta v_{\parallel} + \left(J_{ab}^{\perp}(l, m+1/2) - J_{ab}^{\perp}(l, m-1/2) \right)/\Delta v_{\perp} \quad (57)$$

Where the parallel and perpendicular flux elements in the above equation are calculated from the velocity space integration weights and the flux on the staggered grid via:

$$J_{ab}^{\perp}(l, m \pm 1/2) = \frac{\Delta V_a(m \pm 1/2)}{2\Delta V_a(m)} J_{ab}^{\perp}(l-1/2, m \pm 1/2) + \frac{\Delta V_a(m \pm 1/2)}{\Delta V_a(m)} J_{ab}^{\perp}(l+1/2, m \pm 1/2) \quad (58)$$

$$J_{ab}^{\parallel}(l \pm 1/2, m) = \frac{\Delta V_a(m + 1/2)}{\Delta V_a(m)} J_{ab}^{\parallel}(l \pm 1/2, m + 1/2) + \frac{\Delta V_a(m - 1/2)}{\Delta V_a(m)} J_{ab}^{\parallel}(l \pm 1/2, m - 1/2) \quad (59)$$

All of the fluxes on the staggered grid that fall outside of the simulated velocity space box are set to zero. This enforces the conservation of particles for the differential part of the collision operator.

3.2 Numerical implementation of the integral terms in the collision operator

All of the moments are evaluated with the same numerical integration scheme that is used in the rest of the code:

$$M_{1\mathbf{k}_{\perp}}^{ab} = \int d^3v \frac{m_a v_{\parallel}}{T_a} C_{ab}^{T0}(h_{a\mathbf{k}_{\perp}} J_0(k_{\perp}\rho_a)) = \sum \mathfrak{J}\Delta v_{\parallel}\Delta v_{\perp} \frac{m_a v_{\parallel}}{T_a} C_{ab}^{T0}(h_{a\mathbf{k}_{\perp}} J_0(k_{\perp}\rho_a)) \quad (60)$$

$$M_{2\mathbf{k}_{\perp}}^{ab} = \int d^3v \frac{m_a v_{\parallel}}{T_a} C_{ab}^{T0}(h_{a\mathbf{k}_{\perp}} J_1(k_{\perp}\rho_a)\frac{v_{\perp}}{v_{\parallel}}) = \sum \mathfrak{J}\Delta v_{\parallel}\Delta v_{\perp} \frac{m_a v_{\parallel}}{T_a} C_{ab}^{T0}(h_{a\mathbf{k}_{\perp}} J_1(k_{\perp}\rho_a)v_{\perp}/v_{\parallel}) \quad (61)$$

$$M_{3\mathbf{k}_{\perp}}^{ab} = \int d^3v x_a^2 C_{ab}^{T0}(h_{a\mathbf{k}_{\perp}} J_0(k_{\perp}\rho_a)) = \sum \mathfrak{J}\Delta v_{\parallel}\Delta v_{\perp} x_a^2 C_{ab}^{T0}(h_{a\mathbf{k}_{\perp}} J_0(k_{\perp}\rho_a)) \quad (62)$$

$$M_{4\mathbf{k}_{\perp}}^{ab} = \int d^3v v_{\parallel} J_0(k_{\perp}\rho_a)h_{a\mathbf{k}_{\perp}} = \sum \mathfrak{J}\Delta v_{\parallel}\Delta v_{\perp} v_{\parallel} J_0(k_{\perp}\rho_a)h_{a\mathbf{k}_{\perp}} \quad (63)$$

$$M_{5\mathbf{k}_{\perp}}^{ab} = \int d^3v v_{\perp} J_1(k_{\perp}\rho_a)h_{a\mathbf{k}_{\perp}} = \sum \mathfrak{J}\Delta v_{\parallel}\Delta v_{\perp} v_{\perp} J_1(k_{\perp}\rho_a)h_{a\mathbf{k}_{\perp}} \quad (64)$$

$$M_{6\mathbf{k}_{\perp}}^{ab} = \int d^3v \left(x_a^2 - \frac{3}{2}\right) J_0(k_{\perp}\rho_a)h_{a\mathbf{k}_{\perp}} = \sum \mathfrak{J}\Delta v_{\parallel}\Delta v_{\perp} \left(x_a^2 - \frac{3}{2}\right) J_0(k_{\perp}\rho_a)h_{a\mathbf{k}_{\perp}} \quad (65)$$

Here, $\mathfrak{J}$ represents the Jacobian of velocity space integration. To evaluate these moments, the numerical implementation of C_{ab}^{T0} defined earlier is utilized. This allows for the conservation of momentum and energy to machine precision. In order to more effectively evaluate these moments at every time step, all of the terms which multiply the distribution and Bessel functions are grouped into

10

one set of coefficients. So in the end, in order to evaluate the moments, one simply multiplies the distribution functions, the Bessel functions, and the coefficients, and sums over velocity space.

Now the coefficients of the moments must be considered. The coefficients responsible for maintaining conservation of parallel momentum must be discretized such that the following conservation law is held to machine precision:

$$\int d^3v m_a v_\parallel C_{ab}^T(f_a) + \int d^3v m_b v_\parallel C_{ba}^F(f_a) = 0 \tag{66}$$

To accomplish this, X_1^{ab}, X_4^{ab}, Y_1^{ab}, and Y_4^{ab} are written as:

$$X_1^{ab} = (\theta_{ab} - 1)J_0(k_\perp \rho_a)\frac{T_a F_{Ma} v_\parallel}{m_a \int d^3v F_{Ma} v_\parallel^2} \tag{67}$$

$$X_4^{ab} = -(\theta_{ab} - 1)\frac{\theta_{ab}\alpha_{ab}}{\tau_{ab}\sqrt{1 + \alpha_{ab}^2}}\frac{J_0(k_\perp \rho_a)C_{ab}^{TS}(F_{Ma} m_a v_\parallel/T_a)}{\int d^3v v_\parallel C_{ab}^{TS}(F_{Ma} m_a v_\parallel/T_a)} \tag{68}$$

$$Y_1^{ab} = -J_0(k_\perp \rho_a)\frac{T_b}{T_a}\theta_{ba}\frac{C_{ab}^{TS}(F_{Ma} m_a v_\parallel/T_a)}{\int d^3v C_{ab}^{TS}(F_{Ma} m_a v_\parallel/T_a)m_a v_\parallel/T_a} \tag{69}$$

$$Y_4^{ab} = -\frac{m_b}{T_b\tau_{ba}}\frac{\alpha_{ba}}{\sqrt{1 + \alpha_{ba}^2}}(\theta_{ba} - 1)Y_1^{ab} \tag{70}$$

Provided that the integrations in the above expressions are carried out numerically, and the numerical form of C_{ab}^{T0} is used, momentum will be conserved to machine precision in the drift-kinetic limit. This can be verified by noting that the coefficients of M_1^{ab} and M_4^{ab} cancel when plugged into Eq. (66) (the integral of the differential test-particle part must also be considered when the examining the coefficients of M_1^{ab}). Particles and energy are conserved to machine precision by virtue of the fact that the integration of any term which is odd in $v_\parallel$ is zero. The coefficients responsible for perpendicular momentum conservation are obtained from the parallel momentum coefficients by replacing the $J_0(k_\perp \rho_a)$ Bessel function terms with $J_1(k_\perp \rho_a)v_\perp/v_\parallel$:

$$X_2^{ab} = (\theta_{ab} - 1)J_1(k_\perp \rho_a)\frac{T_a F_{Ma} v_\perp}{m_a \int d^3v F_{Ma} v_\parallel^2} \tag{71}$$

$$X_5^{ab} = -(\theta_{ab} - 1)\frac{\theta_{ab}\alpha_{ab}}{\tau_{ab}\sqrt{1 + \alpha_{ab}^2}}\frac{J_1(k_\perp \rho_a)v_\perp C_{ab}^{TS}(F_{Ma} m_a v_\parallel/T_a)}{v_\parallel \int d^3v v_\parallel C_{ab}^{TS}(F_{Ma} m_a v_\parallel/T_a)} \tag{72}$$

$$Y_2^{ab} = -J_1(k_\perp \rho_a)\frac{T_b}{T_a}\theta_{ba}\frac{v_\perp C_{ab}^{TS}(F_{Ma} m_a v_\parallel/T_a)}{v_\parallel \int d^3v C_{ab}^{TS}(F_{Ma} m_a v_\parallel/T_a)m_a v_\parallel/T_a} \tag{73}$$

$$Y_5^{ab} = -\frac{m_b}{T_b\tau_{ba}}\frac{\alpha_{ba}}{\sqrt{1 + \alpha_{ba}^2}}(\theta_{ba} - 1)Y_2^{ab} \tag{74}$$

Finally, the coefficients responsible for energy conservation must be discretized, where the energy conservation relation for collisions is given by:

$$\int \frac{1}{2}m_a v^2 C_{ab}^T(f_a) + \int d^3v \frac{1}{2}m_b v^2 C_{ba}^F(f_b) = 0 \tag{75}$$

The four coefficients needed for energy conservation can be written as:

$$X_3^{ab} = (\theta_{ab} - 1)\frac{F_{Ma}(x_a^2 - 3/2)J_0(k_\perp \rho_a)}{\int d^3 v F_{Ma} x_a^2 (x_a^2 - 3/2)} \tag{76}$$

$$X_6^{ab} = -(\theta_{ab} - 1)\frac{2\theta_{ab}\alpha_{ab}C_{ab}^{TS}(F_{Ma}x_a^2)J_0(k_\perp \rho_a)}{\tau_{ab}(1 + \alpha_{ab}^2)^{3/2} \int d^3 v x_a^2 C_{ab}^{TS}(F_{Ma}x_a^2)} \tag{77}$$

$$Y_3^{ab} = -J_0(k_\perp \rho_a)\frac{T_b}{T_a}\theta_{ba}\frac{C_{ab}^{TS}(F_{Ma}x_a^2)}{\int d^3 v x_a^2 C_{ab}^{TS}(F_{Ma}x_a^2)} \tag{78}$$

$$Y_6^{ab} = -\frac{2\alpha_{ba}}{\tau_{ba}(1 + \alpha_{ba}^2)^{3/2}}(\theta_{ba} - 1)Y_3^{ab} \tag{79}$$

To make sure particles are conserved to machine precision, the following numerical replacements are made:

$$F_{Ma}(x_a^2 - 3/2) \to F_{Ma}\widetilde{(x_a^2 - 3/2)} = \left(F_{Ma}(x_a^2 - 3/2) - \frac{F_{Ma}}{\int d^3 v F_{Ma}}\int d^3 v F_{Ma}(x_a^2 - 3/2)\right) \tag{80}$$

$$C_{ab}^{TS}(F_{Ma}x_a^2) \to C_{ab}^{TS}\widetilde{(F_{Ma}}x_a^2) = \left(C_{ab}^{TS}(F_{Ma}x_a^2) - \frac{F_{Ma}}{\int d^3 v F_{Ma}}\int d^3 v C_{ab}^{TS}(F_{Ma}x_a^2)\right) \tag{81}$$

The following form is then obtained for the energy conservation coefficients:

$$X_3^{ab} = (\theta_{ab} - 1)\frac{F_{Ma}\widetilde{(x_a^2 - 3/2)}J_0(k_\perp \rho_a)}{\int d^3 v x_a^2 F_{Ma}\widetilde{(x_a^2 - 3/2)}} \tag{82}$$

$$X_6^{ab} = -(\theta_{ab} - 1)\frac{2\theta_{ab}\alpha_{ab}C_{ab}^{TS}\widetilde{(F_{Ma}}x_a^2)J_0(k_\perp \rho_a)}{\tau_{ab}(1 + \alpha_{ab}^2)^{3/2} \int d^3 v x_a^2 C_{ab}^{TS}\widetilde{(F_{Ma}}x_a^2)} \tag{83}$$

$$Y_3^{ab} = -J_0(k_\perp \rho_a)\frac{T_b}{T_a}\theta_{ba}\frac{C_{ab}^{TS}\widetilde{(F_{Ma}}x_a^2)}{\int d^3 v x_a^2 C_{ab}^{TS}\widetilde{(F_{Ma}}x_a^2)} \tag{84}$$

$$Y_6^{ab} = -\frac{2\alpha_{ba}}{\tau_{ba}(1 + \alpha_{ba}^2)^{3/2}}(\theta_{ba} - 1)Y_3^{ab} \tag{85}$$

It is straightforward to show that when the same numerical integration scheme is consistently used, then the above choice of coefficients will conserve energy and particles to machine precision (the proof that energy conservation is numerically satisfied is similar to the proof of momentum conservation). Momentum will be conserved to machine precision, because all terms are even in $v_\parallel$. In the above formulas, the following form for $C_{ab}^{TS}(F_{Ma}m_a v_\parallel / T_a)$ and $C_{ab}^{TS}(F_{Ma}x_a^2)$ are used:

$$C_{ab}^{TS}(F_{Ma}m_a v_\parallel / T_a) = \theta_{ab}\left(C_{ab}^{T0}(F_{Ma}m_a v_\parallel / T_a) - \frac{F_{Ma}m_a \alpha_{ab} v_\parallel(\theta_{ab} - 1)}{\tau_{ab}T_a\sqrt{1 + \alpha_{ab}^2}}\right) \tag{86}$$

$$C_{ab}^{TS}(F_{Ma}x_a^2) = \theta_{ab}\left(C_{ab}^{T0}(F_{Ma}x_a^2) - \frac{2F_{Ma}\alpha_{ab}(\theta_{ab} - 1)}{\tau_{ab}(1 + \alpha_{ab}^2)^{3/2}}(x_a^2 - 3/2)\right) \tag{87}$$

$C_{ab}^{T0}(F_{Ma}m_a v_\parallel / T_a)$ and $C_{ab}^{T0}(F_{Ma}x_a^2)$ are evaluated numerically in the above formulas using the scheme outlined in subsection 3.1.
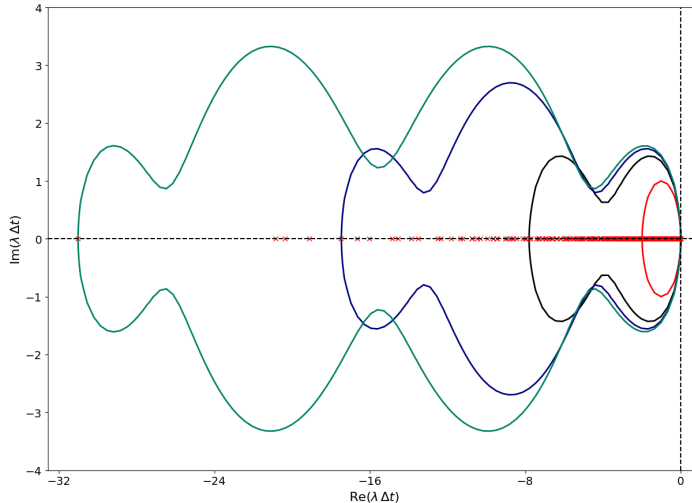
Figure 1: Shapes of stability contours for different stage schemes associated with a given timestep. The eigenvalues of the collision operator (in the drift kinetic limit) are shown by the red crosses. They lie purely along the negative real axis. The stability contours are shown by the curves, and they represent the RKC1 (red), RKC2 (black), RKC3 (blue), and RKC4 (green) time-stepping schemes. As one goes to higher stage schemes, the number of evaluations of the collision operator is increased, and the timestep is also increased. The computational effort associated with all schemes is then evaluated, and the optimal choice is taken [22].

3.3 Explicit time-stepping scheme of collision operator

Since it is expensive to evaluate the collision operator term, and since the collisionality can dramatically limit the timestep in gyrokinetic simulations (especially in the edge), the code is optimized by evolving the collision operator with a separate numerical time scheme than the other terms in the gyrokinetic equation. Currently a first order Runge-Kutta-Chebyshev (RKC) method is employed to evolve the collision operator as opposed to the default 4th order Runge-Kutta schemes used with the other terms, as outlined in [22]. There are four different RKC schemes available in GENE to use with the collision operator, each with a different number of stages (RKC1, RKC2, RKC3, and RKC4). The higher stage schemes require more evaluations and are more expensive to employ. However, they allow for a larger timestep. The lower stage schemes require fewer evaluations. However, they require a smaller timestep. By default, each collisional time-stepping scheme is tested in the initialization phase, and the least computationally expensive scheme is chosen.

Since the collision operator is linear, the eigenvalue spectra of the collision operator can be precomputed and used to determine the maximum possible time step for a given scheme. All of the eigenvalues of the operator must fit within the stability contour for the corresponding time scheme. Fig. 1 shows a plot of the stability contours for the various time-stepping schemes.

Since the contours scale with the timestep, one can optimize the timestep value by ensuring that all of the eigenvalues just barely fit within the stability contours. In all cases, it is the most negative

13

real eigenvalue which determines the timestep. So for a given stage scheme, the most negative real eigenvalue is determined with SLEPc [23, 24], then the stability contour is adjusted (by adjusting the timestep) such that that eigenvalue barely falls within. The corresponding timestep is the optimized one. The computational effort associated with RKC1, RKC2, RKC3, and RKC4 schemes are then compared, and the more optimal choice is used. For practical simulations, such a collisional splitting scheme can improve performance by up to a factor of ~ 3. However, it is desirable to further improve the performance of the splitting scheme because it has been found that even with such a scheme, collisions can highly limit the value of the timestep for simulations in the edge of a magnetic confinement device. Collisional spatial diffusion in particular can dramatically limit the timestep at high k_y. For $k_y \rho_s \sim 10$, the spatial diffusion can shrink the timestep by roughly an order of magnitude, making studies of high k_y gyrokinetic turbulence in the edge impractical until alternative schemes can be employed. For more information, see [22].

3.4 Implementation of collisions with block-structured grids in the velocity space

In addition to the timestep optimization scheme, the collision operator has been adapted to be compatible with the block-structured grid numerical scheme in GENE [16, 17]. Block-structured grids are used to optimize global gyrokinetic simulations (particularly nonlinear simulations) with steep temperature gradients. In turbulent simulations, the perturbed distribution function typically varies on scales of the thermal velocity, $v_T = \sqrt{2T/m}$ in velocity space. So for standard grids, one would need a large velocity-space domain to capture all of the physics in the core, and one would also need a fine velocity space grid to resolve the physics in the edge. This would lead to very expensive high-resolution simulations. One could get around this problem by having a velocity space grid which continuously varied with the radial position as the temperature varied, but this would severely complicate the gyrokinetic equations and numerical model. To get around this problem, the velocity space domain is made to discretely vary with radial position. A typical simulation setup with block-structured grids is shown in Fig. 2.

Block-structured grids are a convenient tool to use with collisions. With block-structured grids, global simulations can be run with fewer velocity space points, which is very convenient for collisional runs, because the computational time to evaluate the collisions increases and the value of the timestep in collisional runs decreases as the number of velocity space points is increased. Furthermore, collisions also help to enforce the assumptions that are made in using the block-structured grid model. The block-structured grid model is predicated on the assumption that the turbulent perturbed distribution function is localized to a structure that varies on the thermal velocity scale. The collisional dissipation function actively drives the perturbation to that sort of structure, providing more confidence that the underlying assumption behind block-structured grids is satisfied. In this way, the two numerical models work to complement each other.

4 Verification Tests

4.1 Relaxation and Conservation Tests

One of the fundamental consequences of the derived collision operator is the relaxation of an arbitrary distribution function towards a perturbed Maxwellian structure of the following form:
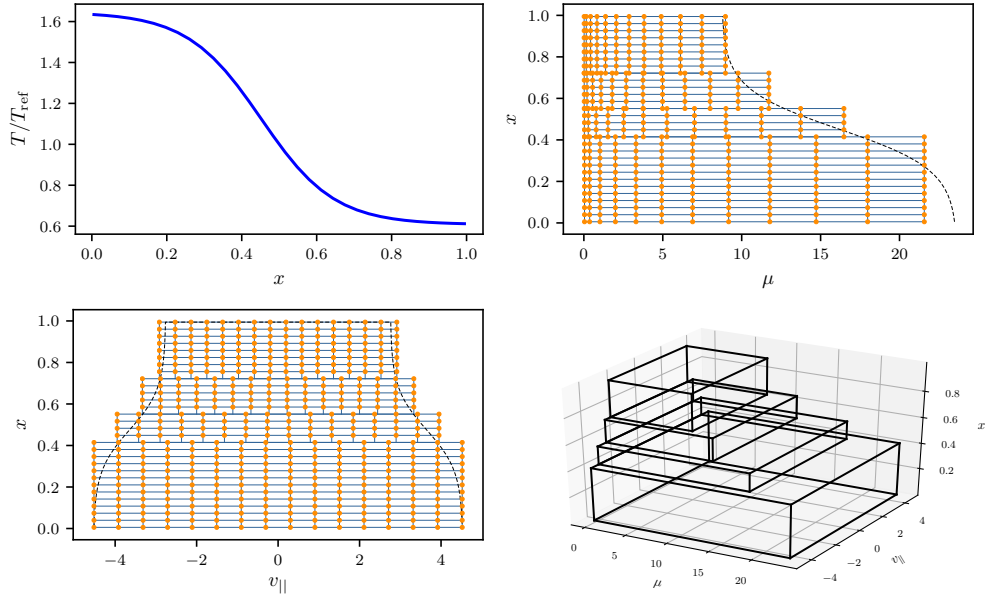
Figure 2: Block-structured grid setup for a typical global simulation with varying temperature profile. The upper-left graph depicts the variation of temperature with radial position. The lower-right plot shows the variation of block sizes with radial position. The larger velocity space boxes are near the core where the thermal speed is higher, and the smaller velocity space boxes are near the edge where the thermal velocity is lower. The lower left plot depicts the variation of the parallel velocity space domain with radial position, and the upper right plot depicts the variation of the magnetic moment velocity space domain with radial position. The above plots used 30 points in the radial position, 24 points in the parallel velocity, and 12 points in the magnetic moment. Typical simulations would require much higher resolution, but the above setup was presented with lower resolution for purposes of clarity.

Species	Mass	Temperature	Density	Charge
Deuterium	1	1	1	1
Boron	5	0.5	0.2	5
Electron	0.0002778	2	2	-1

Table 1: Parameter set for the flow relaxation test. All values in the table are normalized w.r.t. the deuterium values

$$f_a \rightarrow F_{Ma}\left(\frac{\delta n_a}{n_a} + \frac{m_a}{T_a}u_\parallel v_\parallel + \frac{\delta T}{T}\left(x_a^2 - \frac{3}{2}\right)\right) \tag{88}$$

where $u_\parallel$ and $\delta T/T$ are the same between all species after a sufficiently long time. This suggests convenient tests for verifying the correct implementation of the collision operator. One could initialize different species to distributions of the form, $f_a = A_a F_{Ma} v_\parallel$, evolve the species using only the collision operator, and see if all species are driven towards a smooth distribution with the same final flow while verifying that momentum is conserved and the change in free energy is negative definite. Similarly, one could initialize different species to distributions of the form, $f_a = A_a F_{Ma}(x_a^2 - 3/2)$, evolve the species using only the collision operator, and see if all species are driven towards a smooth distribution with the same final perturbed temperature while verifying that particles and energy are conserved and the change in free energy is negative definite. Finally, one can also initialize distributions to arbitrary structures, and verify that the collisions relax such structures to perturbed Maxwellians while maintaining negative definite changes in free energy. These tasks have been done in subsections 4.1.1, 4.1.2, and 4.1.3 respectively. These tests have also been done for nonisothermal parameter sets to verify the correct implementation of the Sugama operator corrections. The standard linearized Landau-Boltzmann collision operator will not pass these tests in the nonisothermal case. All of the quantities are normalized to GENE units. The parameters used in this test are outlined in Table 1. For the following tests, the rate of change of free energy is defined as (all of the quantities are normalized to GENE units):

$$\left.\frac{dF}{dt}\right|_{coll} = \sum_j n_j T_j \int d^3v \frac{h_j}{F_{Mj}} C_j \tag{89}$$

4.1.1 Relaxation of Flow Fluctuations

The derived collision model should act to drive flow perturbations of the form $u_{a\parallel} = \int d^3v v_\parallel f_a/n_a$ towards the same value. To test this property, Deuterium, Boron, and Electron species were initialized to distributions of the form, $f_a = F_{Ma} m_a u_{a\parallel} v_\parallel / T_a$ (where $u_{a\parallel}$ is different for different species), and evolved using only the collision operator in the drift kinetic limit ($k_\perp \rightarrow 0$). The time trace of the flow velocities, free energy dissipation, and momentum conservation error were then examined to verify correct behavior of the collision operator.

The results of the test are shown in Fig. 3, 4, and 5. Fig. 3 shows that the flows for different species all relax to the same value and that the free energy change is negative definite. Fig. 4 shows that the collision operator drives the species towards a smooth final state consistent with the perturbed Maxwellian shape expected. Fig. 5 shows that the momentum conservation error, Δ_M (Eq. (90)), is
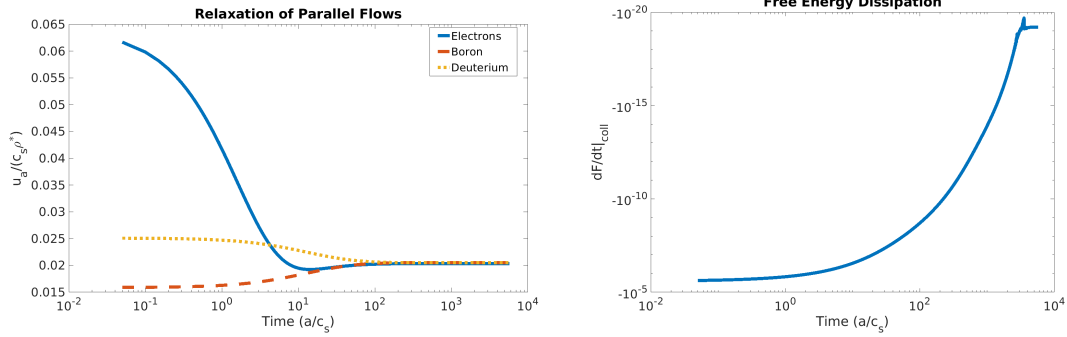
Figure 3: The graph on the left depicts flow equilibration for the relaxation test. Collisions drive all species towards the same parallel flow velocity. The graph on the right depicts free energy dissipation vs. time for the flow relaxation test. The change in free energy by collisions is negative definite, consistent with the second law of thermodynamics.

close to machine precision with a realistic mass ratio system ($< 10^{-10}$). These tests confirm that the collision operator behaves as it should.

$$\Delta_M = \frac{\sum_a m_a \int d^3 v v_\parallel f_a - \left(\sum_a m_a \int d^3 v v_\parallel f_a \right)\Big|_{t=t_{start}}}{\left(\sum_a \int d^3 v v_\parallel f_a \right)\Big|_{t=t_{start}}} \tag{90}$$

4.1.2 Relaxation of thermal fluctuations

The derived collision model should act to drive temperature perturbations of the form $\delta T_a/T_a = \int d^3 v m_a v^2 f_a / 2 n_a$ towards the same value. To test this property, Deuterium, Boron, and Electron species were initialized to distributions of the following form:

$$f_n = \frac{\delta T_n}{T_n} F_{Mn} \left(\frac{m_n v^2}{2 T_n} - \frac{3}{2} \right) \tag{91}$$

where $\delta T_n/T_n$ is different for different species. The system was then evolved using only the collision operator in the drift kinetic limit ($k_\perp \to 0$). The time trace of the temperature fluctuation amplitudes, free energy dissipation, and particle and energy conservation error were then examined to verify correct behavior of the collision operator.

The results of the test are shown in Fig. 6, 7, and 8. Fig. 6 shows that the temperature fluctuations for different species all relax to the same value and that the free energy change is negative definite. Also, the ions equilibrate much faster than the electrons due to the much more similar mass ratio between the two ion species, which is consistent with intuition. Fig. 8 shows that the collision operator drives the species towards a smooth final state consistent with the perturbed Maxwellian shape expected. Fig. 7 shows that the particle and energy conservation error is close to machine precision for a realistic mass ratio system ($< 10^{-10}$) over very long time scales. The expressions for the particle conservation
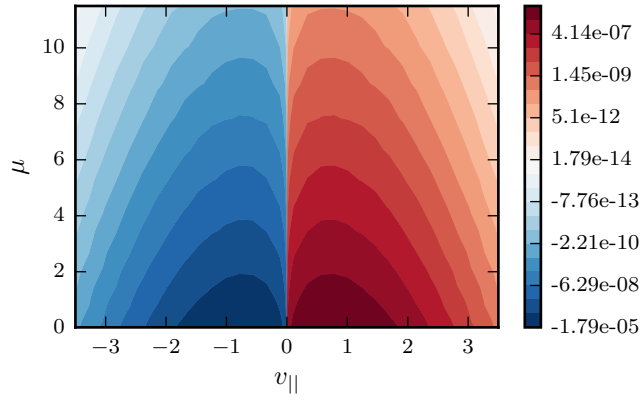
17

Figure 4: Electron velocity space distribution function for the flow relaxation test. Collisions drive all species towards a smooth velocity space distribution resembling the one shown above. The velocity space coordinates are in normalized units. The distribution for Deuterium and Boron look similar.
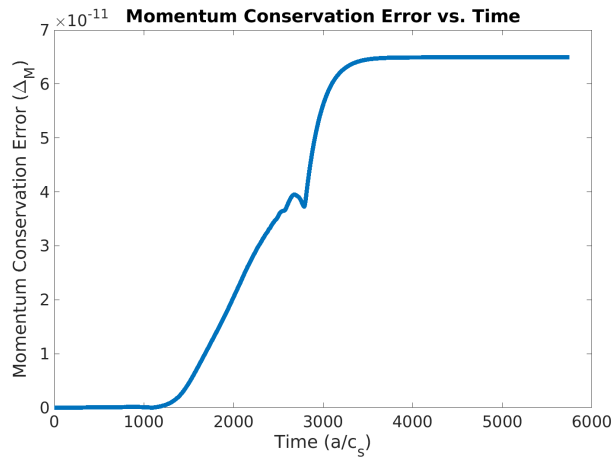

Figure 5: Momentum conservation error vs. time for the flow relaxation test. Collisions conserve momentum to nearly machine precision.
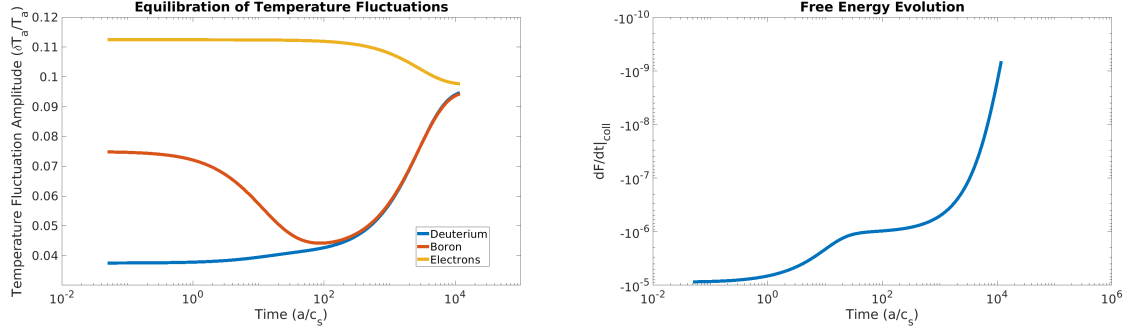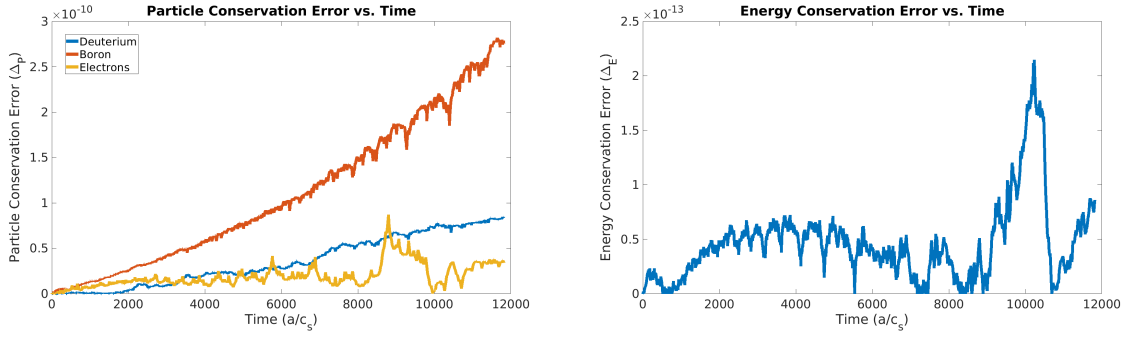
Figure 6: The graph on the left depicts relaxation of temperature fluctuations. The graph on the right depicts free energy dissipation during the relaxation test. The change in free energy due to collisions is negative definite, consistent with the H-theorem.

Figure 7: Particle and energy conservation during the relaxation test. Particles and energy are conserved to nearly machine precision over very long simulation times.

error, Δ_P, energy conservation error, Δ_E, and temperature fluctuation amplitude, $\delta T_a/T_a$, are given in Eq. (92, 93, and 94). These tests confirm that the collision operator behaves as it should.

$$\Delta_P = \frac{\int d^3 v f_a - \left(\int d^3 v f_a\right)\Big|_0}{\left(\int d^3 v f_a\right)\Big|_0} \tag{92}$$

$$\Delta_E = \frac{\sum_a \frac{1}{2} m_a \int d^3 v v^2 f_a - \left(\sum_a \frac{1}{2} m_a \int d^3 v v^2 f_a\right)\Big|_0}{\left(\sum_a \frac{1}{2} m_a \int d^3 v v^2 f_a\right)\Big|_0} \tag{93}$$

$$\frac{\delta T_a}{T_a} = \frac{m_a}{2 n_{a0}} \int d^3 v v^2 f_a/(T_{0a}\rho^*_{ref}) \tag{94}$$

19
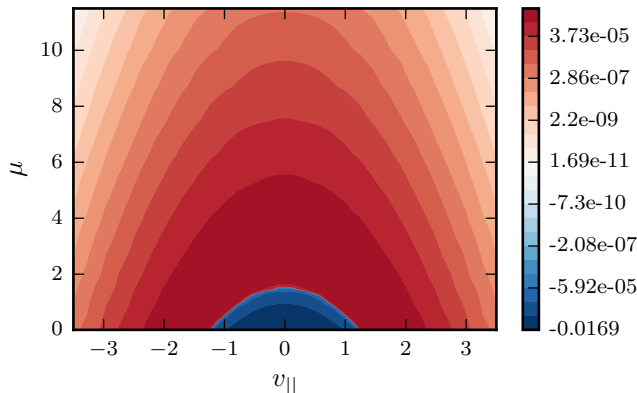
Figure 8: Electron velocity space distribution for temperature fluctuation relaxation test. A similar distribution is obtained for all species.

r/a=0.5	R/a=3	$\hat{s}$=1.0	α=0	q=2.0
$a/L_{Te} = 3$	$a/L_{Ti} = 3$	$a/L_n = 1$	$T_i/T_e = 1$	$m_e/m_i = 0.0002732$

Table 2: General Atomics parameter set [19, 20] for neoclassical benchmark in $\hat{s} - \alpha$ geometry for 2 species case

4.1.3 Relaxation from an arbitrary distribution

In addition to satisfying the simplistic relaxation tests from simple perturbed Maxwellian structures, a relaxation test has been performed where the velocity space profiles for different species have been initialized to arbitrary structures and it has been observed that the H-theorem remains satisfied for this more general scenario, and that the profiles relax to more simple perturbed Maxwellians. Fig. 9 and 10 show the velocity space distributions and the free energy dissipation vs. time for this test.

4.2 Local Neoclassical benchmark

In an effort to further validate the collision operator, local neoclassical simulations have been performed, and the results compared with another neoclassical code, NEO [20, 25]. This code evaluates the neoclassical transport fluxes with the option of using either the full Landau-Boltzmann collision operator (so it does not use approximate model terms in the field-particle part of the operator), or the linearized Landau-Boltzmann collision operator with the model field-particle part (Eq. (7)). Such a comparison has already been performed in [19], but since that time, the collision operator has been rederived and better agreement has been found with the NEO code, particularly for the bootstrap current. Since the full Landau-Boltzmann operator uses a different analytical model for the field-particle part of the collision operator, exact agreement between models should not be expected. However, the results should be relatively close, and the closeness of the results give an indication of the validity of the use of model terms for the field-particle part. The analysis is performed on the same General Atomics parameter set with $\hat{s} - \alpha$ geometry outlined in [19, 20] and displayed in Table 2. The original results from the NEO code have been published in [20].
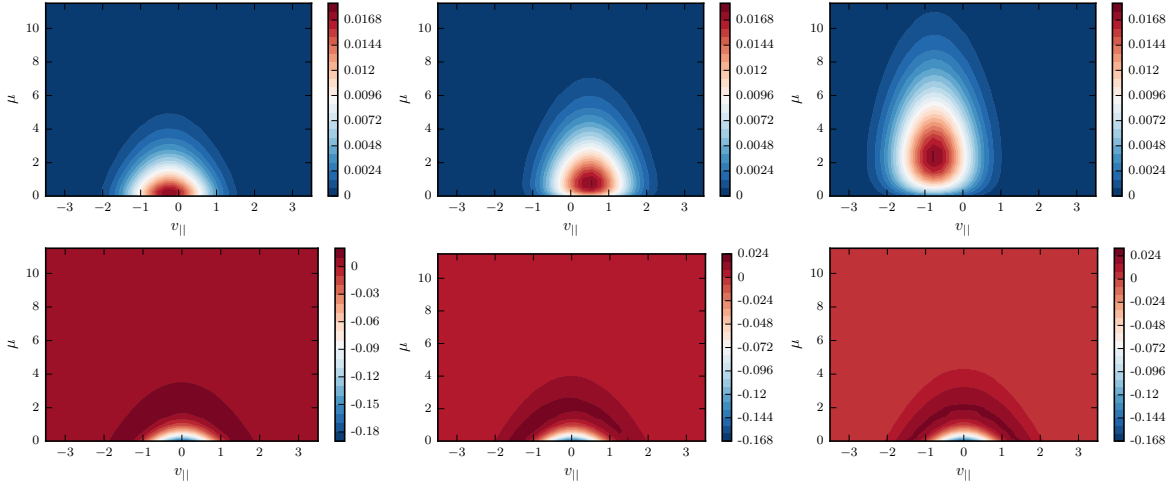
20

Figure 9: Velocity space distribution at the beginning and end of the relaxation test. Collisions relax the distribution to a more localized structure. The graphs at the top are of the initialized distribution, and the graphs at the bottom are of the corresponding final distribution. The graphs on the left, middle, and right correspond to deuterium, boron, and electrons respectively.
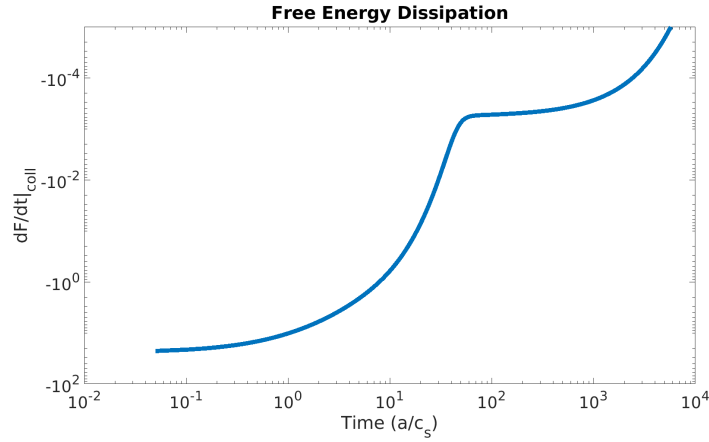

Figure 10: Free energy dissipation for the relaxation test. Free energy dissipation is negative definite, consistent with the second law of thermodynamics.

For the following simulations, the neoclassical heat and particle flux, as well as the bootstrap current were evaluated with the neoclassical solver in a PETSC library [26] that is available in GENE. The collisionality was scanned logarithmically. The comparison could not be extended to higher collisionality due to the computational expense of the neoclassical solver at higher collision frequencies. In practice however, the collision frequency rarely goes to much higher values before the separatrix of the device is encountered. The results of the simulations are displayed in Fig. 11 and 12. By examining the neoclassical equilibrium velocity space distribution at the outboard midplane, one can see the effects of higher collisionality on the ions and electrons. The distributions are displayed in Fig. 13. At low collisionality, the contours of the trapped/passing particle boundary are clearly visible. As the collisionality is raised, the contours are extinguished, which is what is to be expected from intuition, as collisions tend to drive perturbations down towards a perturbed Maxwellian distribution. The collisionality used in the plots is defined in the following equation:

$$\nu_c = \frac{\pi e^4 n_i a \ln(\Lambda)}{2^{3/2} T_i^2} \tag{95}$$

Both GENE and the ad-hoc Fokker Planck model give close agreement, which again suggests that the collision operator in GENE has been implemented correctly. In addition, the ad-hoc model gives relatively close agreement with the full model (the heat and particle fluxes are within $\sim 20\%$). A 20% discrepancy in neoclassical heat transport is relatively small compared to the normal level of turbulent transport, and since neoclassical transport is highly sensitive to collisions, this suggests that the ad-hoc collision model could be justifiably used for studies of collisional plasma turbulence and transport. However, to truly justify the use of such models, a comparison of the microinstabilities and the nonlinear transport between different models should be done.

4.3 Global Neoclassical Benchmark

In addition to the local neoclassical test, a global neoclassical benchmark between GENE and ORB5 [10] has been performed to ensure correct implementation of the collision operator for the global version of the code. The benchmark was performed for a one-species case using a magnetic geometry consisting of concentric circular flux surfaces. The safety factor profile, temperature gradient profile, and density gradient profile are given by the following expressions:

$$q(r) = \left[0.845 + 2.184(r/a)^2\right] \Big/ \sqrt{1 - (r/R)^2} \tag{96}$$

$$\frac{d\ln(T)}{d(r/a)} = -2.49 \left(\cosh(5(r/a - 0.5)) \right)^{-2} \tag{97}$$

$$\frac{d\ln(n)}{d(r/a)} = -0.79 \left(\cosh(5(r/a - 0.5)) \right)^{-2} \tag{98}$$

This benchmark was run with $\nu_i^* = 0.5$ and $\rho^* = 1/180$ with identical analytical collision models, but different numerical implementations. The results are shown in Fig. 14. There is fairly good agreement between GENE and ORB5 for both neoclassical moments, suggesting the collisions were implemented correctly in both codes, at least for the one-species case. The ORB5 data used in this benchmark is published in [10]. Future benchmarks testing the implementation of collisions between multiple species for nonisothermal parameters shall be left for future work.
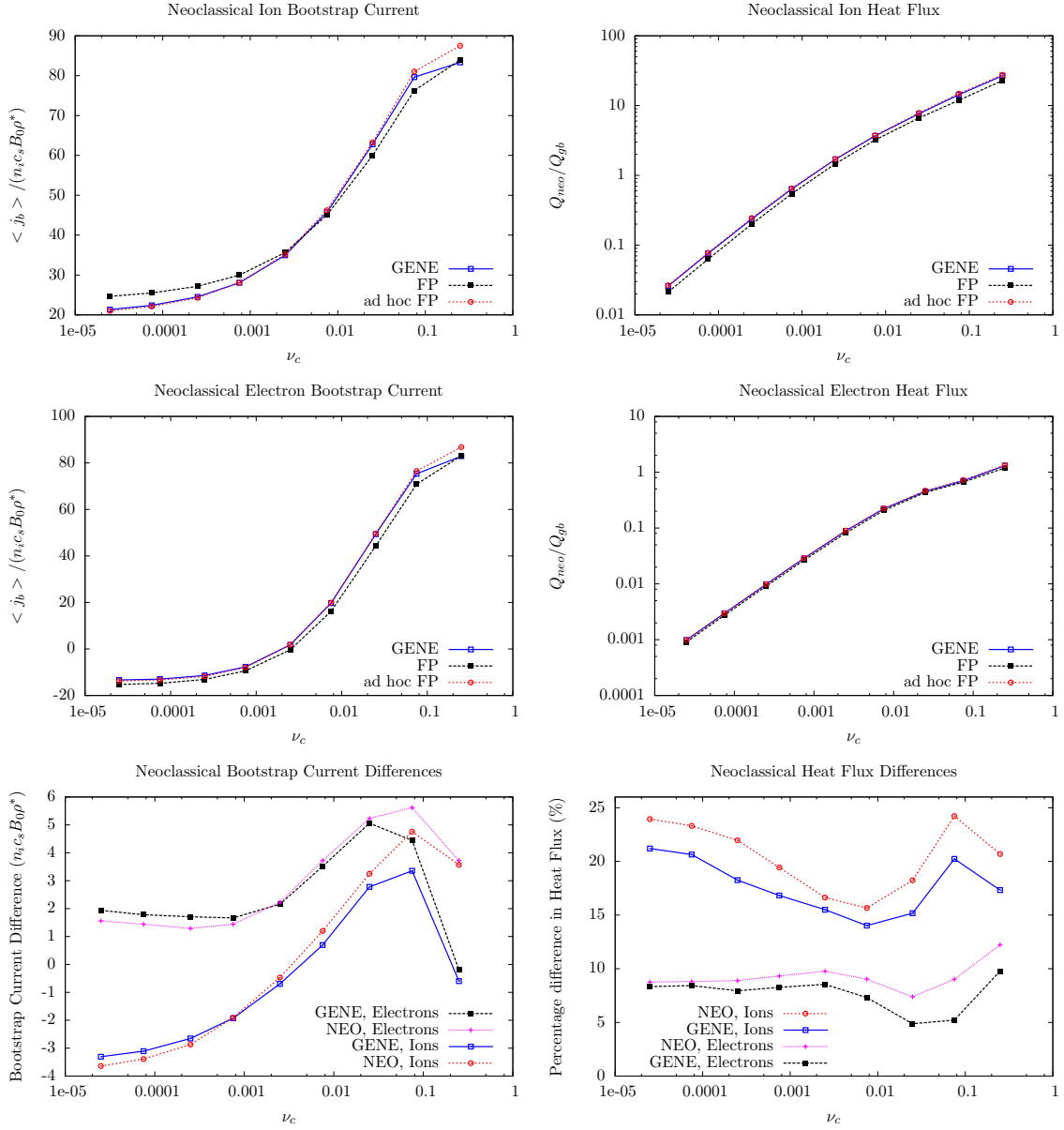
22

Figure 11: Comparison of neoclassical bootstrap current and heat flux between GENE, ad-hoc Fokker-Planck model in NEO, and full Fokker-Planck model in NEO [20]. The bottom plots show the difference of the bootstrap current and heat flux between the model operators and the full operator. GENE predicts a slightly smaller heat flux for ions and electrons, but the agreement is still fairly good. The bootstrap current between the two codes also agree fairly well. Q_{gb} is the gyrobohm heat flux.
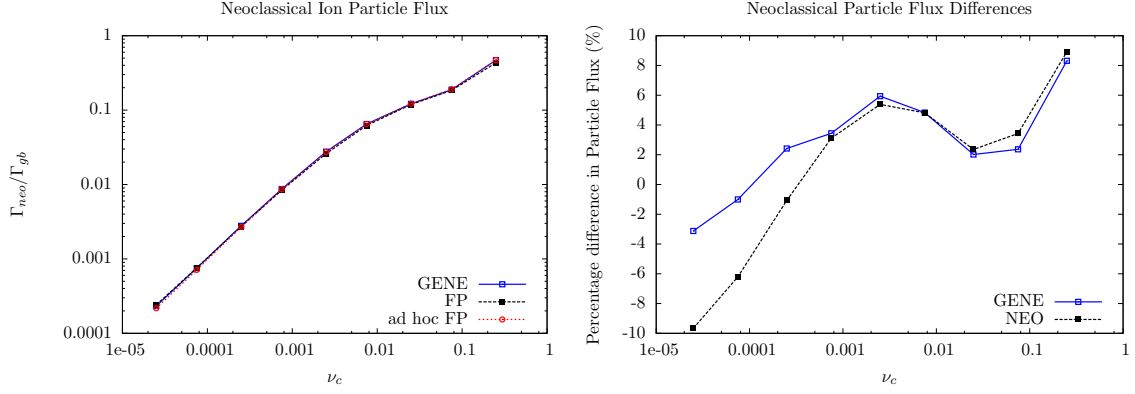
Figure 12: Comparison of neoclassical ion particle flux between GENE, ad-hoc Fokker-Planck model in NEO, and full Fokker-Planck model in NEO [20]. The plot on the right shows the difference in the particle flux between the model operators and the full operator. The electron flux has not been shown because it closely resembles the ion flux. Γ_{gb} is the gyrobohm particle flux.
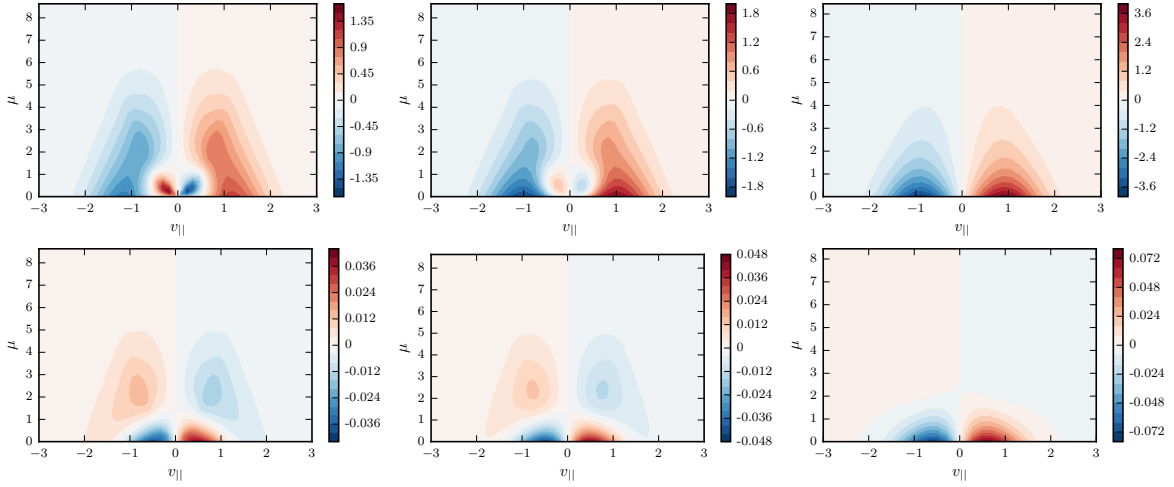
Figure 13: Neoclassical Equilibrium Ion and Electron velocity space distribution at the outboard midplane for coll = 0.00001 (left), coll=0.001 (middle), and coll=0.1 (right). For low collisionality, one can clearly see the complex velocity space contours associated with the trapped-passing boundary. As collisionality is increased, one can see these structures fade as collisions inhibit the trapped particle resonance. At very large collisionality, the contours resemble a simple perturbed Maxwellian structure. The graphs on the top correspond to ions, and the graphs on the bottom correspond to electrons.
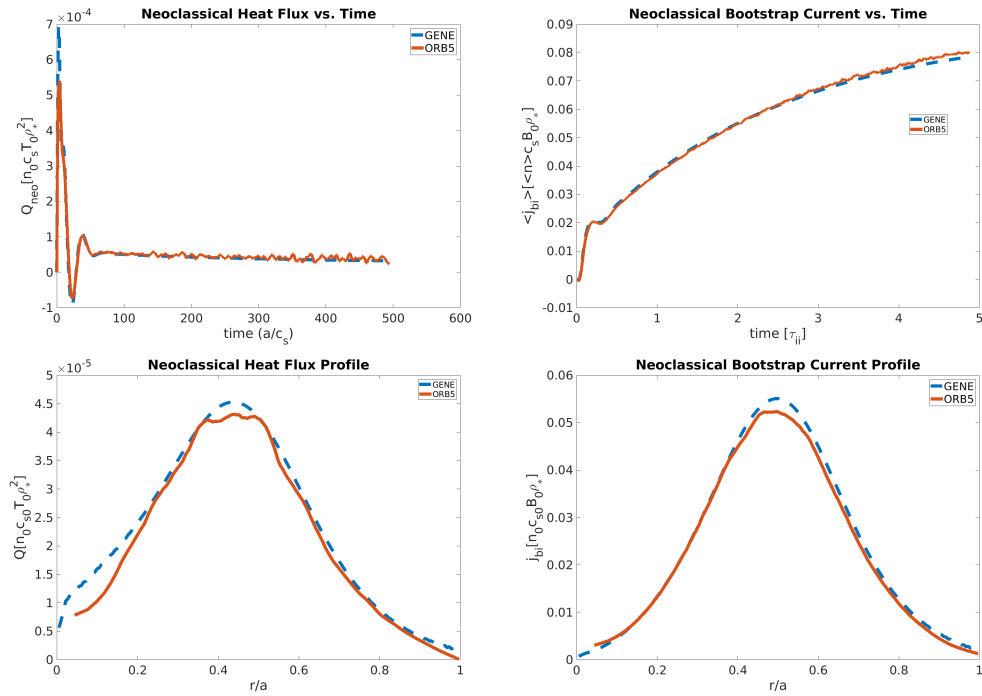
Figure 14: Global Neoclassical Benchmark between GENE and ORB5 [10]. The graphs on the left depict the heat flux, and the graphs on the right depict the bootstrap current. The middle radial position was taken for the time trace (r/a=0.5) and the profile measurements were taken at $t = 2\tau_{ii}$.
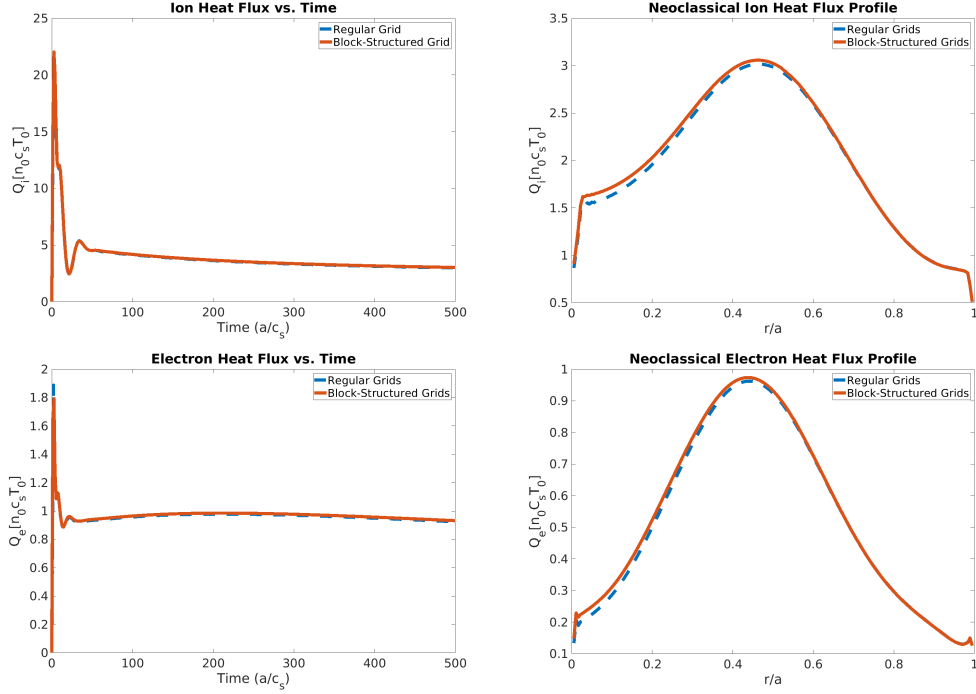
Figure 15: Neoclassical heat flux time trace and profiles for regular and block-structured grids. The graphs on the top and bottom depict the ion and electron species respectively. The time trace depicts the flux-surface averaged heat flux at r/a=0.5, and the profiles were observed at the end of the time trace ($t = 500a/c_s$).

In addition to the benchmark between GENE and ORB5, a two species neoclassical benchmark has been performed between the version of GENE with the standard velocity space grids, and the version of GENE with the block-structured grids. This is done to ensure that the generalization of the numerical scheme to multiple species has been done correctly. The setup for this case is the same as the previous one, except that an additional electron species is considered in the simulation. The heat flux and bootstrap current output is displayed in Fig. 15 and 16 respectively. The neoclassical time traces and profiles agree fairly well between both versions of the code, suggesting that the block-structured grids have been implemented correctly, and provide no significant numerical challenges. Furthermore, introducing these types of grids requires minimal modifications of already existing code.

4.4 Effect of Collisions on Geodesic Acoustic Mode (GAM) oscillations

While neoclassical tests are useful for the verification of the collision operator, it is desirable not just to replicate neoclassical moments, but to incorporate the effect of collisions in simulations of gyrokinetic plasma turbulence. One of the major effects of collisions is the damping of zonal flows, which regulate plasma turbulence by shearing vortices [27]. By failing to replicate the correct level of collisional damping of zonal flows, one would fail to capture the true plasma turbulence and transport. It is essential that the collisional damping rate of zonal flows be modeled correctly. To test that this
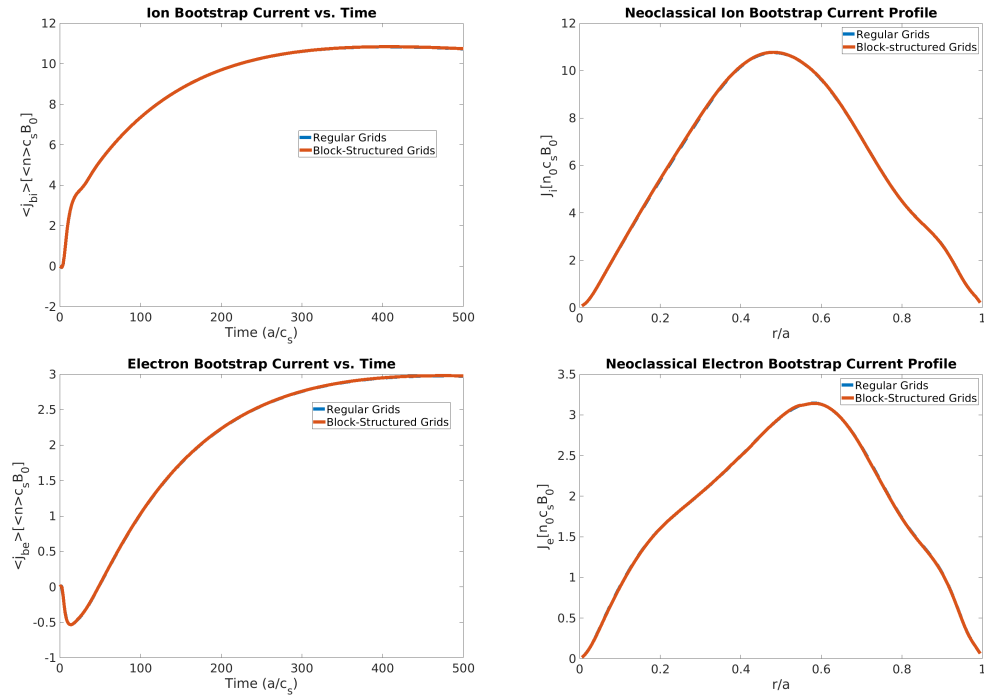
Figure 16: Neoclassical bootstrap current time trace and profiles for regular and block-structured grids. The graphs on the top and bottom depict the ion and electron species respectively. The time trace depicts the flux-surface averaged bootstrap current at r/a=0.5, and the profiles were observed at the end of the time trace ($t = 500a/c_s$).

27

property holds, a simulation has been performed examining the $k_y = 0$ mode, otherwise known as the geodesic acoustic mode (GAM). There is a well established theory of how these modes are dampened by collisions [28]. According to the Rosenbluth-Hinton theory, the short-time behavior of the residual potential in the collisional limit is given by the following formulas:

$$\frac{\phi_k(t)}{\phi_k(0)} \cong A_k(t) + B_k(t) \tag{99}$$

$$A_k(t) = \left(1 - \Lambda\right) \exp\left(-\exp(-q^2)t/(\tau_{ii}R)\right) \cos(t/(\tau_{ii}R)) \tag{100}$$

$$B_k(t) = \Lambda \exp(\Lambda^2 \beta) erfc(\Lambda\sqrt{\beta}) \tag{101}$$

$$\beta = \frac{9\pi^2 q^4 0.61}{\epsilon^2 \ln(16\epsilon\tau_{ii}/(0.61t))^3} \frac{t}{\tau_{ii}} \tag{102}$$

In the above formulas, $A_k(t)$ corresponds to the high frequency GAM oscillation part, $B_k(t)$ corresponds to nonoscillatory part of the potential, Λ is the residual value of the potential in the collisionless limit, q is the safety factor, R is the major radius of the tokamak, ϵ is the inverse aspect ratio for the magnetic geometry, t is time, and τ_{ii} is the ion-ion collision time [29]:

$$\tau_{ii} = \frac{3\sqrt{m_i T_i^3}}{4ne^4 \sqrt{\pi} \ln(\Lambda)} \tag{103}$$

In the above formula, m_i is the ion mass, T_i is the ion temperature, n is the plasma density, e is the ion charge, and $\ln(\Lambda)$ is the Coloumb logarithm. A collisional simulation of GAM oscillations has been performed and the spatially averaged simulated electrostatic potential has been plotted vs. time and compared to $B_k(t)$ to see if the short term collisional decay resembles the prediction by Rosenbluth and Hinton. The results, as well as the parameters of the simulaton, are shown in Fig. 17. It is apparent from the following figure that GENE gives reasonable agreement with the theory of Rosenbluth and Hinton. More information on GAM oscillations can be found in [3, 27, 30].

4.5   Collisional Microinstability Benchmark

In addition to studying the effects of collisions on the damping of zonal flows, the collision operator has also been benchmarked in a local microinstability analysis against the operator in another gyrokinetic code, CGYRO [31]. The $k_y\rho_s$ scan displayed in figure 5 of [32] depicting a trapped electron mode (TEM) has been repeated in GENE. This scenario was based on the General Atomics standard test case, and was run with two species (deuterium and electrons) with no temperature gradients, $a/L_{ni} = a/L_{ne} = 3$, $R/a = 3$, $r/a = 0.5$, $q = 2$, $\hat{s} = 1$, $T_i = T_e$, and $\bar{\nu}_e = \sqrt{2}\pi e^4 a n_e \ln(\Lambda)/(c_s \sqrt{m_e T_e^3}) = 0.2$. The geometry for this scenario is an unshifted miller equilibrium [33, 34]. The results are displayed in Fig. 18. Very good agreement was obtained between the codes. This benchmark in particular, validates the implementation of the FLR correction terms. The CGYRO results are publicly available in Ref. [31].
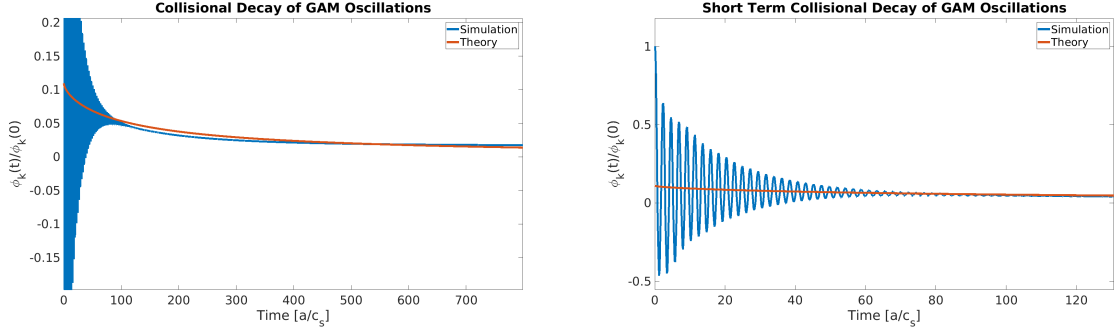
Figure 17: Simulations of collisional GAM oscillations are performed and compared to the short-term decay of the non-oscillatory part of the mode. The above plots demonstrate fairly good agreement between GENE simulations and the theory of Rosenbluth and Hinton [28]. The data for the above graphs was taken from a one species simulation with 48 points in z, 100 points in the magnetic moment, and 200 points in the parallel velocity at $k_x = 0.01$. The size of the velocity space box was 4 and 16 in the parallel velocity and the magnetic moment. The magnetic geometry was circular with a safety factor of 1.4, an inverse aspect ratio of 0.18, and a major radius of 1.0. The ion-ion collision time for the simulation was $\tau_{ii} = 47$ in units of a/c_s.
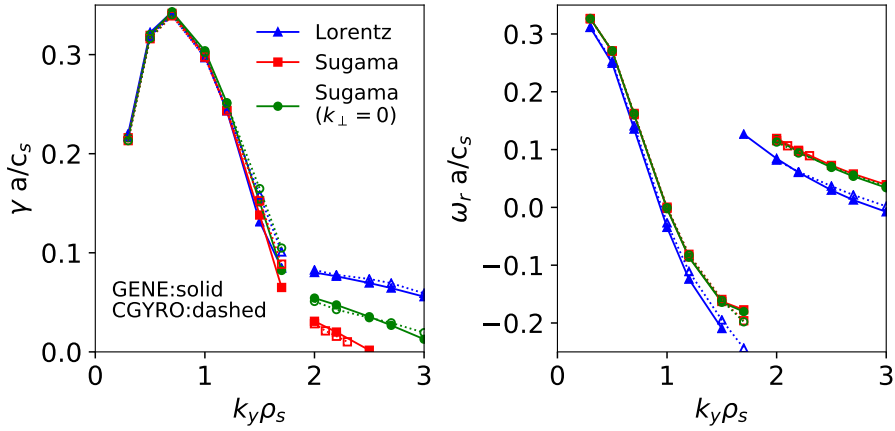

Figure 18: Comparison between GENE and CGYRO [31] of frequencies and growth rates for a TEM microinstability.

5   Conclusion

A new multi-species collision operator based off of a second-order finite volume discretization has been implemented in the GENE code which conserves particles, momentum, and energy to machine precision, and satisfies an appropriate H-theorem such that collisions tend to drive distributions toward perturbed Maxwellian structures. The version of the collision operator implemented for the global version of GENE has also been developed in accordance with the block-structured grid scheme, allowing for more computationally affordable collisional simulations. The collision operator has been validated by confirming that temperature and flow perturbations relax to the same level, confirming that the moments of neoclassical simulations gives close agreement with the NEO and ORB5 codes, confirming that the damping of zonal flows in simulations is close to the theoretical predictions, and benchmarking GENE with CGYRO for a microinstability analysis. This implementation also includes FLR corrections for the local version of the code. Implementing the corrections for the global version of the code shall be left for future work. The developments of the collision operator detailed in this paper enable the study of highly collisional turbulence in the plasma edge.

Acknowledgments

References

[1]   F. Jenko, W. Dorland, M. Kotschenreuther, and B. N. Rogers, Physics of Plasmas **7**, 1904 (2000)

[2]   T. Goerler, X. Lapillonne, S. Brunner, T. Dannert, F. Jenko, F. Merz, D. Told, J. Comput. Phys. **230** (2011) 7053

[3]   H. Sugama, T.-H. Watanabe, and M. Nunami, Physics of Plasmas **16**, 112503 (2009)

[4]   J. Madsen, Phys. Rev. E **87**, 011101 (2013)

[5]   B. Li and D.R. Ernst, Phys. Rev. Lett. **106**, 195002 (2011)

[6]   V. Grandgirard, J. Abiteboul, J. Bigot, T.Cartier-Michaud, N. Crouseilles, G. Dif-Pradalier, Ch. Ehrlacher, D. Esteve, X. Garbet, Ph. Ghendrih, G. Latu, M. Mehrenberger, C. Norscini, Ch. Passeron, F. Rozar, Y. Sarazin, E. Sonnendrucker, A. Strugarek, D. Zarzoso, Comput. Phys. Comm. **207** (2016) 35-68

[7]   I.G. Abel, M. Barnes, S.C. Cowley, W.Dorland, A.A. Schekochihin, Phys. Plasmas **15** (12) (2008) 122509

[8]   F.L. Hinton, R.D. Hazeltine, Rev. Modern Phys. **48** (1976) 239-308

[9] S.P. Hirshman, D.J. Sigmar, Phys. Fluids **19** (10) (1976) 1532-1540

[10] T. Vernay, S. Brunner, L. Villard, B. Mcmillan, O. Sauter, S. Jolliet, T.M. Tran, A. Bottino **260** (2012) 012021

[11] P. Donnel, et al., A multi-species collisional operator for full-F global gyrokinetics codes: Numerical aspects and verification with the GYSELA code, Computer Physics Communications (2018), https://doi.org/10.1016/j.cpc.2018.08.008

[12] R. Hager, E.S. Yoon, S. Ku, E.F. D'Azevedo, P.H. Worley, C.S. Chang, J. Comput. Phys. **315** (2016) 644-660

[13] P. Manas, Y. Camenen, S. Benkadda, W.A. Hornsby, A.G. Peeters, Phys. Plasmas **22** (6) (2015) 062302

[14] M. Nakata, M. Nunami, T.-H. Watanabe, H. Sugama, Computer Physics Communications **197** (2015) 61-72

[15] M. Barnes, I.G. Abel, W. Dorland, D.R. Ernst, G.W. Hammett, P. Ricci, B.N. Rogers, A.A. Schekochihin, T. Tatsuno, Phys. Plasmas **16** (7) (2009) 072107

[16] D. Jarema, H.J. Bungartz, T. Görler, F. Jenko, T. Neckel, D. Told, Computer Physics Communications **215** (2017) 49-62

[17] D. Jarema, H.J. Bungartz, T. Görler, F. Jenko, T. Neckel, D. Told, Computer Physics Communications **198** (2016) 105-117

[18] F. Merz, *Gyrokinetic Simulation of Multimode Plasma Turbulence,* Ph.D. thesis, Westfaelische Wilhelms-Universitaet Muenster (2008)

[19] H. Doerk, *Gyrokinetic Simulation of Microtearing Turbulence,* Ph.D. thesis, Universitaet Ulm (2012)

[20] E.A. Belli and J. Candy, Plasma Phys. Controlled Fusion **54**, 015015 (2012)

[21] A. Bañón Navarro, P. Morel, M. Albrecht-Marc, D. Carati, F. Merz, T. Görler, F. Jenko, Physics of Plasmas **24**, 092303 (2011)

[22] H. Doerk, F. Jenko, Computer Physics Communications **185** (2014) 1938-1946

[23] V. Hernandez, J. E. Roman, and V. Vidal, SLEPc: A Scalable and Flexible Toolkit for the Solution of Eigenvalue Problems , ACM Transactions on Mathematical Software **31**, 351 (2005)

[24] V. Hernandez, J. E. Roman, E. Romero, A. Tomas, and V. Vidal, SLEPc home page , http://www.grycap.upv.es/slepc, 2009

[25] E.A. Belli and J. Candy, Plasma Phys. Controlled Fusion **50**, 095010 (2008)

[26] "http://www.mcs.anl.gov/petsc/" (2012)

[27] P.H. Diamond, S.-I. Itoh, K. Itoh, T.S. Hahm, Plasma Phys. Control. Fusion **47** (5) (2005) R35

[28] F.L. Hinton and M.N. Rosenbluth, *Dynamics of axisymmetric (E x B) and poloidal flows in tokamaks,* Plasma Phys. Control. Fusion **41** (1999)

[29] Braginskii S I 1965 *Reviews of Plasma Physics* vol 1, ed M A Leontovich (New York: Consultants Bureau) p 205

[30] F. Zonca, L. Chen, Europhys. Lett. **83** (3) (2008) 35001

[31] J. Candy, E. Belli, R. Bravenec, Journal of Computational Physics, **324**, 73 (2016)

[32] E.A. Belli and J. Candy, Plasma Phys. Controlled Fusion **59**, 045005 (2017)

[33] R. Miller, M. Chu, J. Greene, Y. Lin-Liu, R. Waltz, Physics of Plasmas, **5**, 973 (1998)

[34] J. Candy, C. Holland, R. Waltz, M. Fahey, E. Belli, Physics of Plasmas, **16**, 060704 (2009)